Journal of Materials Chemistry A

COMMUNICATION

View Article Online
View Journal | View Issue

Cite this: *J. Mater. Chem. A*, 2018, **6**, 24031

Received 12th October 2018
Accepted 4th November 2018

DOI: 10.1039/c8ta09840a

rsc.li/materials-a

$Ti_3C_2T_x$ (T = F, OH) MXene nanosheets: conductive 2D catalysts for ambient electrohydrogenation of N_2 to NH_3†

Jinxiu Zhao,‡[a] Lei Zhang,‡[a] Xiao-Ying Xie,‡[b] Xianghong Li,[a] Yongjun Ma,[c] Qian Liu,*[d] Wei-Hai Fang,[b] Xifeng Shi,[e] Ganglong Cui*[b] and Xuping Sun*[a]

The Haber–Bosch process for industrial-scale NH_3 production suffers from high energy consumption and serious CO_2 emission. Electrochemical N_2 reduction is an attractive carbon-neutral alternative for NH_3 synthesis but is severely restricted due to N_2 activation needing efficient electrocatalysts for the N_2 reduction reaction (NRR) under ambient conditions. Here, we report that $Ti_3C_2T_x$ (T = F, OH) MXene nanosheets act as high-performance 2D NRR electrocatalysts for ambient N_2-to-NH_3 conversion with excellent selectivity. In 0.1 M HCl, such catalysts achieve a large NH_3 yield of 20.4 μg h^{-1} $mg_{cat.}^{-1}$ and a high faradic efficiency of 9.3% at −0.4 V *vs.* reversible hydrogen electrode, with high electrochemical and structural stability. Density functional theory calculations reveal that N_2 chemisorbed on $Ti_3C_2T_x$ experiences elongation/weakness of the N≡N triple bond facilitating its catalytic conversion to NH_3 and the distal NRR mechanism is more favorable with the final reaction of $*NH_2$ to NH_3 as the rate-limiting step.

NH_3 is an essential activated nitrogen source for manufacturing fertilizers, medications, dyes, explosives, resins, *etc.*[1–3] NH_3 is also increasingly regarded as an attractive substitute for petroleum as a transportation fuel having features of high energy density and being free of CO_2 emission.[4] Although N_2 is an inexhaustible molecule in the atmosphere, it is chemically inert owing to its high N≡N bond energy (941 kJ mol^{-1}), low polarizability, and lack of a dipole moment, rendering its conversion to NH_3 difficult.[5–7] Industrial-scale NH_3 production mainly relies on the century-old Haber–Bosch process catalyzed by Fe or Ru using N_2 and H_2 as feeding gases.[8–10] This process however operates at very high temperatures and pressures with serious CO_2 emissions. Thus, it is highly imperative to explore less energy-intensive alternatives for environmentally-benign NH_3 synthesis.

In nature, nitrogenases in bacteria catalyze ambient N_2 fixation through multiple proton and electron transfer steps driven by a significant energy input delivered by ATP.[11–13] Upon the addition of protons and electrons, electrochemical N_2 reduction can also occur under ambient conditions and be powered by renewable energy from solar or wind sources, offering us a promising eco-friendly process for sustainable artificial N_2 fixation.[14–16] Nevertheless, active electrocatalysts for the N_2 reduction reaction (NRR) are needed to address the challenge of N_2 activation. Noble-metal catalysts have been designed to perform NRR with remarkable catalytic performance.[17–20] An immediate outlook for large-scale industrial application points toward the use of systems not relying on expensive precious metals and great recent effort has been put into developing non-noble-metal alternatives.[21–28] Although some progress has been made in this respect, there is still a great need to exploit earth-abundant NRR electrocatalysts which simultaneously achieve large NH_3 yields and high Faradic efficiency (FE).

An ideal NRR electrocatalyst should possess not only a large specific surface area to expose abundant active sites but high electronic conductivity to facilitate efficient electron shuttling. As a new family of 2D materials, MXenes combine the metallic conductivity of transition metal carbides with the hydrophilic nature of their hydroxyl or oxygen terminated surfaces.[29,30] Although MXenes have found widespread application in many field,[31–37] their use for electrocatalytic N_2 reduction has not been explored so far. Herein, we demonstrate the proof of concept that 2D $Ti_3C_2T_x$ (T_x = F, OH) MXene nanosheets ($Ti_3C_2T_x$ NS) perform highly efficiently and stably to electrocatalyze ambient

[a]*Institute of Fundamental and Frontier Sciences, University of Electronic Science and Technology of China, Chengdu 610054, Sichuan, China. E-mail: xpsun@uestc.edu.cn*

[b]*Key Laboratory of Theoretical and Computational Photochemistry, Ministry of Education, College of Chemistry, Beijing Normal University, Beijing 100875, China. E-mail: ganglong.cui@bnu.edu.cn*

[c]*Analytical and Testing Center, Southwest University of Science and Technology, Mianyang 621010, Sichuan, China*

[d]*School of Materials and Energy, University of Electronic Science and Technology of China, Chengdu 611731, Sichuan, China. E-mail: liuqian@uestc.edu.cn*

[e]*College of Chemistry, Chemical Engineering and Materials Science, Shandong Normal University, Jinan 250014, Shandong, China*

† Electronic supplementary information (ESI) available: Experimental section and supplementary figures. See DOI: 10.1039/c8ta09840a

‡ These authors contributed equally to this work.

N_2-to-NH_3 fixation with excellent selectivity, achieving a large NH_3 yield of 20.4 μg h^{-1} $mg_{cat.}^{-1}$ and a high FE of 9.3% at −0.4 V *vs.* reversible hydrogen electrode (RHE). The NRR mechanism is also studied using density functional theory (DFT) calculations, which suggest that the final electrocatalytic reaction of $*NH_2 \rightarrow NH_3$ is the rate-limiting step.

$Ti_3C_2T_x$ NSs were prepared according to previous reports (see ESI for preparative details†).[32,38] As seen from the X-ray diffraction (XRD) patterns (Fig. 1a), the (002) diffraction peak shifts to a lower angle and the most intense peak of Ti_3AlC_2 at $2\theta \approx 39°$ disappears, showing successful conversion of Ti_3AlC_2 to $Ti_3C_2T_x$.[38] From the scanning electron microscopy (SEM) images of bulk Ti_3AlC_2 (Fig. S1†) and delaminated $Ti_3C_2T_x$ NSs (Fig. 1b), it is clearly seen that bulk Ti_3AlC_2 was converted to a loosely layered $Ti_3C_2T_x$ structure after the etch reactions. The nanosheet nature of $Ti_3C_2T_x$ is evidenced by the transmission electron microscopy (TEM) image shown in Fig. 1c. The high-resolution TEM (HRTEM) image (Fig. 1d) reveals lattice fringes with a layer distance of 0.91 nm, which is in good agreement with previous reports.[32] The EDX spectrum (Fig. S2†) indicates the presence of Ti, C, O, and F. TEM and corresponding energy-dispersive X-ray (EDX) elemental mapping images confirm the uniform distribution of all four elements within $Ti_3C_2T_x$ (Fig. 1e).

The X-ray photoelectron spectroscopy (XPS) survey spectrum also confirms the presence of Ti, C, O, and F in $Ti_3C_2T_x$, as shown in Fig. S3.† In the Ti 2p region (Fig. 2a), both Ti $2p_{3/2}$ and Ti $2p_{1/2}$ can be fitted with five peaks,[39] corresponding to the Ti–C bond, Ti(II), Ti(III), TiO_2, and Ti–F bond, respectively. The C 1s region (Fig. 2b) is deconvoluted into five peaks at binding energies (BEs) of 281.7, 284.4, 286.2, 288.2, and 290.9 eV, which are assigned to Ti–C, C–C, C–O, HO–C=O, and C–F bonds,

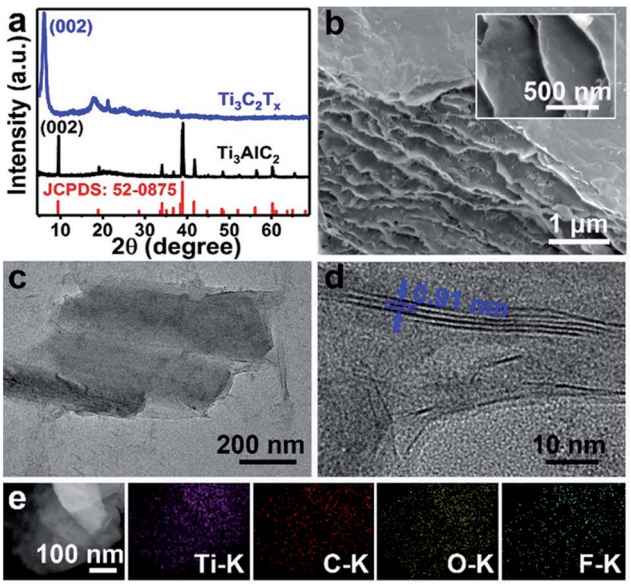

Fig. 1 (a) XRD patterns of Ti_3AlC_2 and $Ti_3C_2T_x$. (b) SEM images of $Ti_3C_2T_x$. (c) TEM and (d) HRTEM images of $Ti_3C_2T_x$ NSs. (e) TEM and corresponding EDX elemental mapping images of Ti, C, O, and F for $Ti_3C_2T_x$ NSs.

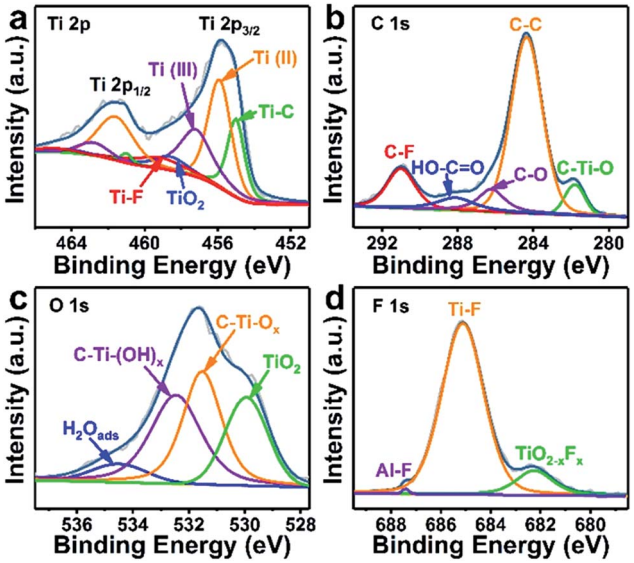

Fig. 2 XPS spectra of $Ti_3C_2T_x$ in the (a) Ti 2p, (b) C 1s, (c) O 1s, and (d) F 1s regions.

respectively.[40–43] In the O 1s region (Fig. 2c), the BEs at 529.9, 531.5, 532.4, and 533.9 eV are derived from O–Ti, C–Ti–O, C–Ti–$(OH)_x$, and H–O–H bonds, respectively.[41,43–45] Fig. 2d shows $TiO_{2-x}F_x$ and Ti–F signals at BEs of 682.1 and 685.0 eV, respectively,[40,43–45] and the small peak occurring at 687.5 eV can be assigned to Al–F.[41] All these observations support the successful preparation of $Ti_3C_2T_x$ nanosheets.

The electrochemical measurements were performed in a gas-tight two-compartment cell separated by a piece of Nafion 211 membrane. $Ti_3C_2T_x$ was deposited on carbon paper ($Ti_3C_2T_x$/CP, $Ti_3C_2T_x$ loading: 0.2 mg cm^{-2}) as the working electrode with the use of Ag/AgCl as the reference in the cathode chamber and graphite plate as the counter electrode in the anode chamber. During electrolysis, N_2 gas was bubbled onto the cathode, where protons transported through the electrolyte (0.1 M HCl aqueous solution) can react with N_2 on the surface of the catalyst to produce NH_3. All the potentials for NRR were reported on a RHE scale. Fig. 3a displays the time-dependent current density curves of $Ti_3C_2T_x$/CP in 0.1 M HCl electrolyte for 2 h, as the potential shifts from −0.35 to −0.55 V. The obtained NH_3 in the solution phase was spectrophotometrically determined using the indophenol blue method,[46] and another possible by-product (N_2H_4) was detected using the method of Watt and Chrisp.[47] The corresponding calibration curves are shown in Fig. S5 and S6†. Fig. S7† shows the UV-vis absorption spectra of the electrolytes stained with p-$C_9H_{11}NO$ indicator after NRR electrolysis at a series of potentials, indicating the excellent selectivity of $Ti_3C_2T_x$/CP for NH_3 production. Fig. 3b presents the UV-vis absorption spectra of electrolytes coloured with indophenol indicator after 2 h electrocatalytic reaction at a series of potentials, and the electrolyte shows the highest absorbance intensity when electrolyzed at −0.40 V. NH_3 yield and corresponding FE at various potentials were calculated and are plotted in Fig. 3c. Both NH_3 yield and FE increase when the

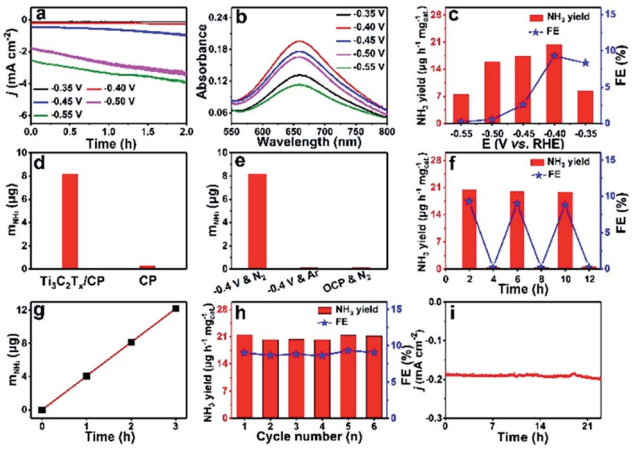

Fig. 3 (a) Time-dependent current density curves for $Ti_3C_2T_x$/CP at different potentials in 0.1 M HCl. (b) UV-vis absorption spectra of the 0.1 M HCl electrolytes stained with indophenol indicator after electrolysis at a series of potentials. (c) NH_3 yields and FEs at each given potential. (d) Amount of produced NH_3 for $Ti_3C_2T_x$/CP and bare CP after 2 h electrolysis. (e) Amount of produced NH_3 for $Ti_3C_2T_x$/CP under different test conditions. (f) NH_3 yields and FEs for $Ti_3C_2T_x$/CP with alternating 2 h cycles between N_2-saturated and Ar-saturated electrolytes. (g) Amount of produced NH_3 *vs.* time recorded at −0.4 V. (h) Stability test of $Ti_3C_2T_x$/CP during repeated NRR at −0.4 V. (i) Time-dependent current density curve for $Ti_3C_2T_x$/CP at −0.4 V for 23 h.

negative potential increased from −0.35 to −0.40 V. At −0.40 V, this catalyst is capable of achieving a large NH_3 yield of 20.4 μg h^{-1} $mg_{cat.}^{-1}$ (4.08 μg h^{-1} $cm_{cat.}^{-2}$) and a high FE of 9.3%, comparing favourably to the behaviour of most reported aqueous-based NRR electrocatalysts under ambient conditions, including Au NRs (1.64 μg h^{-1} $cm_{cat.}^{-2}$, 3.88%),[18] Fe_2O_3–CNT (0.22 μg h^{-1} $cm_{cat.}^{-2}$, 0.15%),[21] Fe_2O_3/Ti (3.43 μg h^{-1} $cm_{cat.}^{-2}$, 2.6%),[24] *etc.* A more detailed comparison is shown in Table S1.† The decrease of both NH_3 yield and FE was observed as the potential negatively shifted to −0.55 V, which is attributed to the competitive adsorption of N_2 and hydrogen species on the electrode surface.[48–50] It should be mentioned that bare CP has poor NRR activity (Fig. 3d). We also explored the influence of catalyst loading on NRR performance and found that 0.2 mg was the optimum mass loading for NRR (Fig. S7†).

To further verify that the product was indeed generated *via* N_2 reduction electrocatalyzed by $Ti_3C_2T_x$/CP, three control experiments were conducted: (1) $Ti_3C_2T_x$/CP in N_2-saturated solution at an open-circuit potential (OCP) for 2 h; (2) $Ti_3C_2T_x$/CP in Ar-saturated solution at −0.40 V for 2 h; (3) $Ti_3C_2T_x$/CP at −0.40 V with alternating 2 h cycles between N_2- and Ar-saturated solutions. No NH_3 was detected in control experiments (1) and (2), as shown in Fig. 3e. For the last control experiment, NH_3 was only obtained in N_2-saturated solution at −0.40 V (Fig. 3f). Furthermore, there is a linear correlation between the amount of produced NH_3 and the time within 3 h electrolysis (Fig. 3g). In addition, we conducted electrocatalytic NRR in 0.05 M H_2SO_4 and 0.1 M Na_2SO_4. Results suggested that $Ti_3C_2T_x$ was efficient for NRR under both of these conditions (Fig. S8 and S9†).

Stability is another critical parameter for the practical application of catalysts. After 6 consecutive cycles, both NH_3 yield rate and FE show small variations (Fig. 3h). After 23 h NRR electrolysis, our $Ti_3C_2T_x$/CP still maintains strong long-term electrochemical durability with little attenuation in current, as shown in Fig. 3i. XRD (Fig. S10†) and XPS (Fig. S11†) data confirm that $Ti_3C_2T_x$ has no obvious changes in crystalline phase and valence states. The TEM image shows the preservation of nanosheet features for post-NRR $Ti_3C_2T_x$ (Fig. S12†) after NRR electrolysis. These results imply high structural stability.

To gain further insight into the active sites and electrocatalytic processes of NRR on $Ti_3C_2T_x$, we performed DFT calculations to explore the atomistic electrocatalytic NRR mechanism on the $Ti_3C_2T_x$ model. Since N_2 adsorption on the catalyst surface is the first process for NRR, its initial adsorption configurations are very important for the following electrocatalytic reactions. For our $Ti_3C_2T_x$ model, the end-on and side-on adsorption structures were optimized and found to be stable (Fig. 4). The adsorption energy of the end-on configuration was a little smaller than that of the side-on one (potential energy: 0.80 *vs.* 1.00 eV; free energy: 0.37 *vs.* 0.46 eV). In these adsorption structures, the N–N bond length is elongated very much, and was calculated to be 1.194 and 1.268 angstrom for the end-on and side-on adsorption structures, respectively. Obviously, the elongated N–N bond length is proportional to the adsorption energy. In other words, the larger the adsorption energy is, the longer the N–N bond length becomes.

In the following calculations we started from the side-on adsorption structure to explore its subsequent electrocatalytic NRR mechanism on the $Ti_3C_2T_x$ surface. Fig. 4 shows our calculated favorable energy profiles for NRR on the $Ti_3C_2T_x$ surface (optimized structures are shown in Fig. S13†). In the distal mechanism, the whole reaction is divided into two half reactions. First, protons and electrons attack a terminal nitrogen atom to generate a NH_3 molecule; then, the remaining nitrogen atom is hydrogenated to form another NH_3 molecule. The first half reaction is exothermic by 2.68 eV free energy from the N_2 to *N species. In contrast, the second half reaction is energetically uphill except the first reaction from *N to *NH.

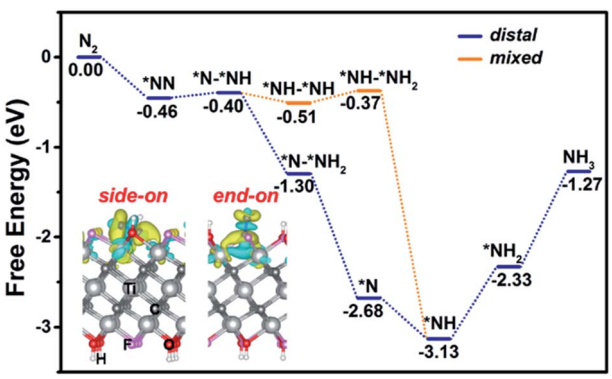

Fig. 4 DFT calculated energy profile for electrocatalytic N_2 reduction reaction on $Ti_3C_2T_x$. The charge density difference of the two adsorption configurations is also shown. Yellow and blue represent charge accumulation and depletion (isovalue: 0.005 au).

The rate-limiting step is the final $*NH_2$ to NH_3 reaction. In addition, we also calculated the alternative NRR mechanism, which was found to be energetically unfavorable (Fig. S13 and S14†). Instead, we have found another energetically allowed mixed NRR mechanism (Fig. 4). In this mechanism, the first reaction steps *i.e.* from N_2 to *NH–*NH_2 are the same as those in the alternative mechanism. The difference is that in the mixed one, a proton and electron pair is added to the $*NH_2$ moiety of the *NH–*NH_2 species generating a NH_3 molecule, not the *NH moiety. As a result, the high-energy NH_2–NH_2 intermediate is bypassed. This is also consistent with the experimental observation of not detecting the N_2H_4 species (see above). It should be noted that both distal and mixed mechanisms have the same rate-limiting step. Nonetheless, the distal mechanism is still preferred because of its much more significant exothermicity from *N–*NH to *NH (Fig. 4).

In summary, $Ti_3C_2T_x$ MXene nanosheets have been experimentally and theoretically verified as non-noble-metal 2D catalysts to enable high-performance electrohydrogenation of N_2 to NH_3 under ambient conditions. When tested in acids, this catalyst is excellent in activity with a NH_3 yield of 20.4 μg h^{-1} $mg_{cat.}{}^{-1}$ and a FE of 9.3%, with high electrochemical and structural stability. DFT calculations reveal that the distal NRR mechanism is more favorable and the related $*NH_2 \rightarrow NH_3$ reaction is the rate-limiting step. This study not only provides us with an attractive earth-abundant catalyst material for electrochemical NH_3 synthesis, but it would open up exciting new avenues for the rational design and development of MXene-based nanocatalysts for artificial N_2 fixation.

Conflicts of interest

There are no conflicts to declare.

Acknowledgements

This work was supported by the National Natural Science Foundation of China (No. 21575137).

References

1 V. Smil, *Nature*, 1999, **400**, 415.
2 R. Schlögl, *Angew. Chem., Int. Ed.*, 2003, **42**, 2004–2008.
3 V. Rosca, M. Duca, M. T. de Groot and M. T. Koper, *Chem. Rev.*, 2009, **109**, 2209–2244.
4 T. Vegge, R. Z. Sørensen, A. Klerke, J. S. Hummelshøj, T. Johannessen, J. K. Nørskov and C. H. Christensen, *Indirect Hydrogen Storage in Metal Ammines*, British Welding Research Association, 2008, pp. 533–564.
5 M. D. Fryzuk, J. B. Love, S. J. Rettig and V. G. Young, *Science*, 1997, **275**, 1445–1447.
6 A. R. Singh, B. A. Rohr, J. A. Schwalbe, M. Cargnello, K. Chan, T. F. Jaramillo, I. Chorkendorff and J. K. Nørskov, *ACS Catal.*, 2017, **7**, 706–709.
7 H. Jia and E. A. Quadrelli, *Chem. Soc. Rev.*, 2014, **43**, 547–564.
8 G. Ertl, *Catalytic Ammonia Synthesis*, ed. J. R. Jennings, Plenum, New York, 1991.
9 I. Dybkjaer in *Ammonia, Catalysis and Manufacture*, ed. A. Nielsen, Springer, Heidelberg, 1995, pp. 199–308.
10 M. Appl, *Ammonia–Ullmann's Encyclopedia of Industrial Chemistry*, Wiley-VCH Verlag GmbH & Co. KGaA, 2002.
11 M. K. Chan, J. Kim and D. C. Rees, *Science*, 1993, **260**, 792–794.
12 B. K. Burgess and D. J. Lowe, *Chem. Rev.*, 1996, **96**, 2983–3011.
13 K. A. Brown, D. F. Harris, M. B. Wilker, A. Rasmussen, N. Khadka, H. Hamby, S. Keable, G. Dukovic, J. W. Peters, L. C. Seefeldt and P. W. King, *Science*, 2016, **352**, 448–450.
14 C. J. M. van der Ham, M. T. M. Koper and D. G. H. Hetterscheid, *Chem. Soc. Rev.*, 2014, **43**, 5183–5191.
15 V. Kyriakou, I. Garagounis, E. Vasileiou, A. Vourros and M. Stoukides, *Catal. Today*, 2017, **286**, 2–13.
16 C. Guo, J. Ran, A. Vasileff and S. Qiao, *Energy Environ. Sci.*, 2018, **11**, 45–56.
17 M. Shi, D. Bao, B. R. Wulan, Y. Li, Y. Zhang, J. Yan and Q. Jiang, *Adv. Mater.*, 2017, **29**, 1606550.
18 D. Bao, Q. Zhang, F. Meng, H. Zhong, M. Shi, Y. Zhang, J. Yan, Q. Jiang and X. Zhang, *Adv. Mater.*, 2017, **29**, 1604799.
19 H. Huang, L. Xia, X. Shi, A. M. Asiri and X. Sun, *Chem. Commun.*, 2018, **54**, 11427–11430.
20 J. Wang, L. Yu, L. Hu, G. Chen, H. Xin and X. Feng, *Nat. Commun.*, 2018, **9**, 1795.
21 Z. Wang, F. Gong, L. Zhang, R. Wang, L. Ji, Q. Liu, Y. Luo, H. Guo, Y. Li, P. Gao, X. Shi, B. Li, B. Tang and X. Sun, *Adv. Sci.*, 2018, **5**, 1801182.
22 X. Zhang, Q. Liu, X. Shi, A. M. Asiri, Y. Luo, X. Sun and T. Li, *J. Mater. Chem. A*, 2018, **6**, 17303–17306.
23 Y. Zhang, W.-B. Qiu, Y. Ma, Y. Luo, Z. Tian, G. Cui, F. Xie, L. Chen, T. Li and X. Sun, *ACS Catal.*, 2018, **8**, 8540–8544.
24 Q. Liu, X. Zhang, B. Zhang, Y. Luo, G. Cui, F. Xie and X. Sun, *Nanoscale*, 2018, **10**, 14386–14389.
25 L. Zhang, X. Ji, X. Ren, Y. Ma, X. Shi, Z. Tian, A. M. Asiri, L. Chen, B. Tang and X. Sun, *Adv. Mater.*, 2018, **30**, 1800191.
26 L. Zhang, X. Ji, X. Ren, Y. Luo, X. Shi, A. M. Asiri, B. Zheng and X. Sun, *ACS Sustainable Chem. Eng.*, 2018, **6**, 9550–9554.
27 X. Wu, L. Xia, Y. Wang, W. Lu, Q. Liu, X. Shi and X. Sun, *Small*, 2018, **14**, 180311.
28 R. Zhang, Y. Zhang, X. Ren, G. Cui, A. M. Asiri, B. Zheng and X. Sun, *ACS Sustainable Chem. Eng.*, 2018, **6**, 9545–9549.
29 M. Naguib, V. N. Mochalin, M. W. Barsoum and Y. Gogotsi, *Adv. Mater.*, 2014, **26**, 992–1005.
30 B. Anasori, M. R. Lukatskaya and Y. Gogotsi, *Nat. Rev. Mater.*, 2017, **2**, 16098.
31 M. R. Lukatskaya, O. Mashtalir, C. E. Ren, Y. Dall'Agnese, P. Rozier, P. L. Taberna, M. Naguib, P. Simon, M. W. Barsoum and Y. Gogotsi, *Science*, 2013, **341**, 1502–1505.
32 M. Ghidiu, M. R. Lukatskaya, M. Q. Zhao, Y. Gogotsi and M. W. Barsoum, *Nature*, 2014, **516**, 78–81.
33 F. Shahzad, M. Alhabeb, C. B. Hatter, B. Anasori, S. M. Hong, C. M. Koo and Y. Gogotsi, *Science*, 2016, **353**, 1137–1140.
34 H. Liu, C. Duan, C. Yang, W. Shen, F. Wang and Z. Zhu, *Sens. Actuators, B*, 2015, **218**, 60–66.

35 Q. Peng, J. Guo, Q. Zhang, J. Xiang, B. Liu, A. Zhou, R. Liu and Y. Tian, *J. Am. Chem. Soc.*, 2014, **136**, 4113–4116.
36 X. Wu, Z. Wang, M. Yu, L. Xiu and J. Qiu, *Adv. Mater.*, 2017, **29**, 1607017.
37 T. Ma, J. Cao, M. Jaroniec and S. Qiao, *Angew. Chem., Int. Ed.*, 2016, **55**, 1138–1142.
38 O. Mashtalir, M. Naguib, V. N. Mochalin, Y. Dall'Agnese, M. Heon, M. W. Barsoum and Y. Gogotsi, *Nat. Commun.*, 2013, **4**, 1716.
39 O. Mashtalir, K. M. Cook, V. N. Mochalin, M. Crowe, M. W. Barsoum and Y. Gogotsi, *J. Mater. Chem. A*, 2014, **2**, 14334–14338.
40 B.-S. Shen, H. Wang, L.-J. Wu, R.-S. Guo, Q. Huang and X.-B. Yan, *Chin. Chem. Lett.*, 2016, **27**, 1586–1591.
41 Y. Cao, Q. Deng, Z. Liu, D. Shen, T. Wang, Q. Huang, S. Du, N. Jiang, C.-T. Lin and J. Yu, *RSC Adv.*, 2017, **7**, 20494–20501.
42 J. Yan, C. E. Ren, K. Maleski, C. B. Hatter, B. Anasori, P. Urbankowski, A. Sarycheva and Y. Gogotsi, *Adv. Funct. Mater.*, 2017, **27**, 1701264.
43 J. Halim, K. M. Cook, M. Naguib, P. Eklund, Y. Gogotsi, J. Rosen and M. W. Barsoum, *Appl. Surf. Sci.*, 2016, **362**, 406–417.
44 H. Wang, J. Zhang, Y. Wu, H. Huang and Q. Jiang, *J. Phys. Chem. Solids*, 2018, **115**, 172–179.
45 Q. Fu, J. Wen, N. Zhang, L. Wu, M. Zhang, S. Lin, H. Gao and X. Zhang, *RSC Adv.*, 2017, **7**, 11998–12005.
46 D. Zhu, L. Zhang, R. E. Ruther and R. J. Hamers, *Nat. Mater.*, 2013, **12**, 836–841.
47 G. W. Watt and J. D. Chrisp, *Anal. Chem.*, 1952, **24**, 2006–2008.
48 X. Ren, G. Cui, L. Chen, F. Xie, Q. Wei, Z. Tian and X. Sun, *Chem. Commun.*, 2018, **54**, 8474–8477.
49 J. Han, Z. Liu, Y. Ma, G. Cui, F. Xie, F. Wang, Y. Wu, S. Gao, Y. Xu and X. Sun, *Nano Energy*, 2018, **52**, 264–270.
50 W. Qiu, X. Xie, J. Qiu, W. Fang, R. Liang, X. Ren, X. Ji, G. Cui, A. M. Asiri, G. Cui, B. Tang and X. Sun, *Nat. Commun.*, 2018, **9**, 3485.